RSC Chemical Biology

Accepted Manuscript

This article can be cited before page numbers have been issued, to do this please use: B. Biswas, J. Zhuo, J. Bosch, H. Vu, L. Pak, R. Raja, A. Roy, A. Panattoni, M. Maryska, P. Slavík, K. Šigut, A. R. Fehr, R. Abraham, B. Slusher, T. Tsukamoto and A. Leung, *RSC Chem. Biol.*, 2026, DOI: 10.1039/D6CB00139D.

ROYAL SOCIETY OF CHEMISTRY

rsc.li/rsc-chembio

View Article Online
DOI: 10.1039/D6CB00139D

View Article Online
DOI: 10.1039/D6CB00139D

Cellular Engagement of the SARS-CoV-2 Macrodomain by GS-441524 and Enhanced In Vitro Inhibition by its Diphosphorylated Metabolite

Banhi Biswas[1†*], Junlin Zhuo[1 †], Jürgen Bosch[2,3], Hien Vu[1], Lorencia Pak[1], Rameez Raja[1], Anuradha Roy[4], Alessandro Panattoni[5], Michal Maryska[5], Petr Slavik[5], Kryštof Šigut[5], Anthony R. Fehr[6], Rachy Abraham[1], Barbara S. Slusher[7,8], Takashi Tsukamoto[7,8], Anthony K. L. Leung[1,9,10,11*]

[1] Department of Biochemistry and Molecular Biology, Bloomberg School of Public Health, Johns Hopkins University, Baltimore, Maryland, United States

[2] Center for Global Health and Diseases, Case Western Reserve University, Cleveland, Ohio, United States

[3] InterRayBio, LLC, Cleveland, Ohio, United States

[4] High Throughput Screening Laboratory, Del M. Shankel Structural Biology Center, Kansas, Lawrence, United States

[5] SigutLabs, Praha, Czech Republic

[6]Department of Molecular Biosciences, University of Kansas, Lawrence, United States

[7] Department of Neurology, Johns Hopkins University School of Medicine, Baltimore, Maryland, United States

[8]Johns Hopkins Drug Discovery, Johns Hopkins University School of Medicine, Baltimore, Maryland, United States

[9] Department of Molecular Biology and Genetics, Johns Hopkins University, Baltimore, Maryland, US

[10] McKusick-Nathans Department of Genetic Medicine, Johns Hopkins University, Baltimore, Maryland, United States

[11] Department of Oncology, School of Medicine, Johns Hopkins University, Baltimore, Maryland, United States

*Corresponding authors, Email: anthony.leung@jhu.edu, bbiswas1@jh.edu

[†] These authors contributed equally to the work

Abstract

View Article Online
DOI: 10.1039/D6CB00139D

Coronavirus macrodomains (Mac1) counter host immunity by removing ADP-ribose. GS-441524, the parent nucleoside of remdesivir, inhibits SARS-CoV-2 Mac1, but its active metabolite and cellular engagement were undefined. GS-441524 selectively inhibits SARS-CoV-2 Mac1 over human MacroD2, engages Mac1 in cells but not MERS-CoV Mac1, with its diphosphate metabolite being most potent.

View Article Online
DOI: 10.1039/D6CB00139D

Introduction

Macrodomains are conserved protein modules present in both host and viral proteins that regulate ADP-ribosylation, a post-translational modification catalyzed by ADP-ribosyltransferases, commonly known as PARPs, through the addition of one or more ADP-ribose units to proteins (1). Certain PARPs are upregulated during viral infection as interferon (IFN)-stimulated genes, and their overexpression can inhibit the replication of coronaviruses, alphaviruses, and other RNA viruses (2–5). To counter this host defense, certain positive-stranded RNA viruses—including alphaviruses, coronaviruses, rubella virus, and hepatitis E virus—encode macrodomains that remove ADP-ribosylation, thereby evading host immune responses (3,4,6–8).

In coronaviruses, the nonstructural protein 3 typically contains two or three macrodomains. Mutations within the first macrodomain (Mac1) — such as those in SARS-CoV-2 — that disrupt ADP-ribose binding or hydrolysis significantly reduce viral pathogenesis, virulence, and disease severity in mouse infection models (9–11). Although SARS-CoV-2 viruses lacking Mac1 can still be recovered in cell culture, Mac1-deleted MERS-CoV and MHV viruses are non-viable (9). Together, these findings establish the coronavirus macrodomain, Mac1, as a compelling target for antiviral drug development.

Following the onset of the COVID-19 pandemic, considerable efforts have been made to develop small-molecule inhibitors of the SARS-CoV-2 macrodomains (12–17). GS-441524, the parent nucleoside of remdesivir and one of the earliest nucleoside analogs tested against SARS-CoV-2, not only inhibits viral RNA polymerase but also binds the viral macrodomain with an affinity comparable to ADP-ribose (18–20). Previous gel-based assays demonstrated that GS-441524 inhibits SARS-CoV-2 macrodomain hydrolase activity in a semi-quantitative manner (19). Here, using a high-throughput ADP-ribosylhydrolase assay (ADPr-Glo) (21), we show that GS-441524 selectively inhibits SARS-CoV-2 Mac1 (IC_{50} = 14.35 μM) but not its closest human homolog, MacroD2, and demonstrate for the first time its direct engagement with Mac1 in cells.

GS-441524 is metabolized intracellularly to its mono-, di-, and triphosphate forms, with the triphosphate serving as the inhibitor of the RNA-dependent RNA polymerase of SARS-CoV-2 (22–25). However, it remains unclear which metabolite mediates macrodomain inhibition. Systematic evaluation of its phosphorylated derivatives identifies the diphosphate metabolite as the most potent inhibitor, revealing a distinct structure–activity relationship from that governing polymerase inhibition.

Main text

GS-441524 selectively blocks the hydrolase activity of SARS-CoV-2 Mac1

View Article Online
DOI: 10.1039/D6CB00139D

GS-441524 binds the SARS-CoV-2 Mac1 with an affinity close to its native substrate, ADP-ribose (18,19). Using a time-dependent semiquantitative immunoblot assay, previous studies indicate that GS-441524 can also inhibit the hydrolase activity of Mac1 (19). In this study, we employed a high-throughput, quantitative luminescence-based assay, ADPr-Glo (21), to evaluate whether GS-441524 inhibits the hydrolase activity of SARS-CoV-2 Mac1 (Figure 1A). Briefly, ADP-ribosylated PARP10 catalytic domain was incubated with Mac1 in the presence or absence of GS-441524. The ADP-ribose released from the substrate by Mac1 was subsequently hydrolyzed by the phosphodiesterase NudF to generate AMP, which was quantified using the AMP-Glo assay. We found that GS-441524 significantly inhibited SARS-CoV-2 Mac1 with an IC_{50} of 14.35 μM (Figure 1B). However, it did not inhibit the closest human macrodomain homolog, MacroD2, indicating viral selectivity. Consistent with this selectivity, a previous study also reported that GS-441524 does not bind to two other human macrodomains (19).

To evaluate the breadth of inhibition, we examined GS-441524 against another coronavirus macrodomain (MERS-CoV Mac1) and extended testing to an alphavirus macrodomain from Chikungunya virus. Among these, GS-441524 was most active against SARS-CoV-2 Mac1, showing modest inhibition of SARS-CoV Mac1 (IC_{50} = 63 μM), weak inhibition of CHIKV macrodomain (IC_{50} = 218 μM), and no inhibition of MERS-CoV Mac1 (Figure 1B). The greater similarity between SARS-CoV and SARS-CoV-2 Mac1—both members of the Sarbecovirus subgenus of Betacoronavirus—likely accounts for their comparable sensitivities, whereas MERS-CoV, a Merbecovirus, is more divergent (26). The variation in inhibition among viral macrodomains may reflect differences in the surrounding loop regions that shape the active-site pocket, despite conservation of key catalytic residues (19). The selectivity of GS-441524 for SARS-CoV-2 Mac1 over the human homolog MacroD2 may further stem from differences in electrostatic surface potential and pocket size between the two macrodomains (21). Together, these structural and electrostatic differences likely underlie the preferential inhibition of SARS-CoV-2 Mac1 by GS-441524.

GS-441524 engages with the SARS-CoV-2 Mac1 in cells

Although several studies have examined the binding and inhibition of GS-441524 on the SARS-CoV-2 macrodomain in vitro (18–20), whether this interaction occurs in cells remains unknown. To evaluate its cellular engagement, we performed a cellular thermal shift assay (CETSA). In this assay, Mac1 was fused to a HiBiT tag, a small peptide complement of NanoLuc luciferase (nLuc). Cells transiently expressing Mac1–HiBiT were treated with GS-441524 and exposed to a temperature gradient. After lysis, the soluble fraction of Mac1 was quantified by complementing HiBiT with the large NanoLuc

View Article Online
DOI: 10.1039/D6CB00139D

fragment (LgBiT), generating a luminescent signal proportional to the amount of soluble protein (Figure 1C) (15,27).

GS-441524 treatment increased the aggregation temperature T_{agg}—the temperature at which 50% of the protein remains soluble—of SARS-CoV-2 Mac1 in a dose-dependent manner. At 100 μM, GS-441524 elevated the T_{agg} by 1.7 °C, and at 250 μM, by 3.62 °C, indicating enhanced thermal stability of Mac1 in the presence of the compound (Figure 1D). This stabilization demonstrates that GS-441524 directly engages the SARS-CoV-2 macrodomain in cells (Figure 1D).

Western blot analysis of soluble protein fractions further confirmed increased solubility at higher temperatures compared with the DMSO control. We performed western analysis of SARS-CoV-2 Mac1 with different doses of GS-441524 and at different temperatures. Consistent with the luciferase-based CETSA results, a similar dose-dependent stabilization was observed by western blotting: treatment with 100 μM and 250 μM GS-441524 at 41.6 °C resulted in ~2-fold and ~4-fold increase in solubility, respectively (Figure 1E). Notably, when parallel luciferase-based and western blot CETSA analyses were performed for MERS-CoV Mac1, no dose-dependent stabilization was observed—consistent with its lack of inhibition in the in vitro ADPr-Glo assay (Figure 1D-E, S1).

These findings demonstrate that GS-441524 engages the SARS-CoV-2 macrodomain in cells, albeit with lower potency than observed in vitro. This difference may reflect the use of an isolated, soluble Mac1 domain rather than the full-length, membrane-associated nsp3 protein in which Mac1 resides. Moreover, evaluating Mac1 engagement during infection is complicated by the fact that GS-441524 is metabolized intracellularly to its triphosphate form, which potently inhibits the viral RNA-dependent RNA polymerase at nanomolar concentrations (24). By contrast, macrodomain interaction occurs at micromolar levels and is therefore unlikely to contribute directly to antiviral efficacy under these conditions. Nevertheless, these findings reveal that GS-441524 and its derivatives can interact with two essential viral proteins, suggesting opportunities to design next-generation derivatives with optimized dual-target antiviral activity.

The diphosphate derivative of GS-441524 is more potent than GS-441524

Given that GS-441524 is metabolized intracellularly to its mono-, di-, and triphosphate forms (GS-MP, GS-DP, and GS-TP) (Figure 2A), we next examined whether these phosphorylated derivatives differ in their ability to bind and stabilize the SARS-CoV-2 macrodomain. Using an AlphaScreen with a non-hydrolyzable ADP-ribosylated peptide (28), GS-DP exhibited the strongest binding to SARS-CoV-2 Mac1 (IC_{50} = 1.01 μM)

View Article Online
DOI: 10.1039/D6CB00139D

compared to GS-441524 (IC_{50} = 8.3 μM) (Figure 2B). Parallel differential scanning fluorimetry analyses showed a consistent trend, with GS-DP producing the largest shift in T_m compared to GS-441524 and the other phosphorylated derivatives across different concentrations of the compounds (Figure 2C).

Because GS-441524 derivatives structurally resemble phosphorylated adenine nucleotides, which could interfere with signal detection in the ADPr-Glo assay, we confirmed inhibitory activity using an orthogonal, gel-based hydrolase assay. GS-DP demonstrated substantially greater inhibition than GS-441524, while GS-MP and GS-TP displayed comparable potency to the parent compound (Figure 2D, E, S2). Together, these results establish the diphosphate form as the most potent GS-441524 metabolite for Mac1 inhibition.

Docking reveals the structural basis for enhanced inhibition by GS-441524 diphosphate

The SARS-CoV-2 Mac1 active site pocket is highly flexible and can accommodate a diverse set of ligands (12–14,18). ADP-ribose (ADPr) binds to Mac1 through distinct subsites: 1) Adenosine subsite (blue) – the adenine base forms hydrogen bonds with D22 and I23; 2) Phosphate tunnel (yellow) – the diphosphate moiety interacts with V49, G130, I131, and F132; 3) Distal ribose site (pink) – the distal ribose contacts N40, K44, G46, G48, and F132 (via van der Waals interactions); and 4) Oxyanion subsite (red) – the proximal ribose engages F156 and D157 through a bridging water (Figure 3A) (13,14,29) .

The pyrrolotriazine ring of GS-441524 occupies the adenosine subsite, while its 1′-nitrile group (–CN) extends into the oxyanion pocket, without forming direct contacts with F156 or D157 (18). Addition of a phosphate group, as in GS-MP, modestly improves Mac1 binding affinity (18)

To understand the mechanism underlying the increased potency of GS-DP, we performed molecular docking studies with SARS-CoV-2 Mac1. We first assessed whether our docking could accurately reproduce experimentally observed binding geometries. We evaluated the agreement between the docked poses and the crystallographic coordinates of GS-441524 (PDB: 7BF6) by superimposing the predicted and observed SARS-CoV-2 Mac1 structures using PyMOL (30), and measuring the atomic distances between the docked and crystallographic poses. The root-mean-square deviation (RMSD) between the docked pose and the crystal structure of GS-441524 was 2.5 Å across 18 atoms, indicating strong concordance between the docking protocol and the experimentally determined binding mode (Figure S3A). The largest difference was a flip of the hydroxymethyloxolane (ribose), which likely reflects the absence of explicit water molecules in the docking protocol. In contrast, the

View Article Online
DOI: 10.1039/D6CB00139D

pyrrolotriazine ring itself shifted by less than 1 Å, preserving the key contacts (Figure S3B). Based on this validation, we proceeded to dock GS-DP into the SARS-CoV-2 Mac1 binding site. Molecular docking provides a rationale for the enhanced inhibition observed with GS-DP. The diphosphate moiety of GS-DP extends into the Mac1 phosphate tunnel, forming additional hydrogen bonds with V49, G130, I131, and F132—closely mimicking ADPr interactions (Figure 3B–D). These extra contacts likely underlie its superior binding and inhibition. Additionally, GS-441524 (orange) formed a hydrogen bond with the backbone of A154, adopting a slightly different orientation compared to the ligand surface representation of GS-DP (blue), which overlapped with the ADPr (black) shape of a known crystal structure (PDB 7CZ4) (Figure 3E).

Comparison of the C_α root-mean-square deviations (RMSD) of Mac1 docked with GS-441524 or GS-DP relative to the ADPr-bound structure (PDB 7CZ4) revealed the largest backbone shifts in the G96–L107 region (β5–α4 loop), with RMSD values of 0.3–1.4 Å for GS-441524 and 0.1–0.8 Å for GS-DP. Smaller deviations were observed in the G46–G48 activation loop (~0.5 Å for both). Notably, the L126–I136 region (β6–α5 loop) that accommodates the diphosphate of ADPr showed marked displacement in the GS-441524 complex but not in GS-DP, supporting the insertion of GS-DP's diphosphate group into the phosphate tunnel (Figure 3F).

Although GS-DP exhibited stronger Mac1 inhibition in vitro, its high negative charge likely limits cellular permeability, precluding direct antiviral application. Future chemical modifications to enhance membrane permeability will be essential for therapeutic development.

Conclusions

Although GS-441524 is well established as an antiviral targeting the viral polymerase, its mechanism of macrodomain inhibition has remained unclear—particularly which intracellular metabolite mediates this activity and whether Mac1 is engaged in cells. Here, we address both questions by systematically evaluating GS-441524 and its phosphorylated derivatives.

In contrast to structure-guided optimization strategies that modify nucleotide scaffolds to enhance binding affinity(31), our work focuses on the endogenous metabolic derivatives of GS-441524. By systematically evaluating these intracellular forms, we identify the diphosphate metabolite (GS-DP) as the most active species, revealing a previously underappreciated role for intermediate nucleotide states in macrodomain inhibition. This contrasts with the triphosphate form responsible for polymerase inhibition and highlights distinct structure–activity relationships across viral targets. Recent studies have reported GS-441524-derived diphosphate–ribose analogs with nanomolar binding

View Article Online
DOI: 10.1039/D6CB00139D

affinity (20,32), as well as selective Mac1 inhibitors derived from monophosphate-based scaffolds(31). Together, these complementary approaches highlight both the potential of synthetic optimization and the role of endogenous metabolites in shaping macrodomain inhibitor activity.

While prior studies have characterized GS-441524 binding and inhibition of viral macrodomains in vitro (18,19), whether this interaction occurs in cells has remained unresolved. Using CETSA, we demonstrate that GS-441524 directly engages the SARS-CoV-2 macrodomain in a cellular environment. Combined with quantitative comparison across viral and human macrodomains, our results establish selective targeting of SARS-CoV-2 Mac1 and highlight functional divergence among macrodomains.

Molecular docking suggests that the enhanced activity of GS-DP arises from additional interactions within the phosphate tunnel that mimic those of ADP-ribose, while the 1′-nitrile group of GS-441524 contributes to viral selectivity through engagement of the oxyanion subsite, a position incompatible with its closest human homolog MacroD2 (20). Consistent with prior structural studies, the oxyanion subsite remains a preferred binding region for many Mac1 inhibitors(12–14).

By identifying the diphosphate metabolite as the most potent inhibitory species and elucidating its structural basis of interaction, this work provides a framework for the development of next-generation macrodomain inhibitors. More broadly, these findings suggest that intracellular nucleotide metabolism can be leveraged to generate active species with distinct target specificities, raising the possibility of designing nucleoside analogs that differentially engage viral polymerase and macrodomain functions.

Methods

Proteins and chemicals

SARS-CoV-2 Mac1, CHIKV-nsp3^{MD}, MERS-CoV Mac1, NudF, and PARP10 catalytic domains were purified in-house as previously described. GS-441524 was purchased from MedChem Express. The phosphorylated derivatives of GS-441524 were synthesized as detailed in the supplementary information.

Automodification of PARP10

PARP10 peptide was ADP-ribosylated as previously described (25) with some modifications. Briefly, His-SUMO attached to the PARP10-derived sequence CRRPVEQVLYH peptide (20μM) was incubated with NAD+ (600μM) and PARP10 Catalytic Domain (1μM) in 50mM HEPES, 150mM NaCl, and 1mM TCEP overnight at room temperature. ADP-ribosylated-HisSUMO-PARP10-derived peptide was purified

View Article Online
DOI: 10.1039/D6CB00139D

with Ni-NTA, concentrated, aliquoted, and stored at -80 °C. The concentration was measured using absorbance at 260 nm.

ADPr-Glo assay

ADPr-Glo assay protocol (21) was used to evaluate the inhibitory activity of GS-441524 against viral and human macrodomains. Briefly, the linear activity range of each macrodomain was determined before dose–response assays. GS-441524 was diluted to the desired concentrations in 2% (v/v) DMSO and preincubated with NudF ADP-ribose pyrophosphatase (125 nM) and either SARS-CoV-2 Mac1 (2 nM), MERS-CoV Mac1 (8 nM), SARS-CoV Mac1 (2 nM), Chikungunya virus macrodomain (37.5 nM), or human MacroD2 (2 nM) in a 384-well plate. Reactions were initiated by adding 20 μM mono-ADP-ribosylated peptide substrate and incubated at room temperature for 30 minutes. Reaction products were quantified using the AMP-Glo kit, which converts AMP generated from ADP-ribose hydrolysis into luminescent signals.

Gel-based orthogonal assay with SARS-CoV-2 Mac1 inhibitors

SARS-CoV-2 Mac1 (250 nM) was preincubated with compounds (555 μM, 2.2% DMSO) on ice for 30 minutes in a reaction buffer containing 50mM HEPES, pH 7.2, 150mM NaCl, 0.2 mM DTT, and 0.02% v/v NP-40. 10 μM ADP-ribosylated PARP10 catalytic domain was added to the reaction and incubated at 37℃ for 1 hour. The reaction was terminated by adding 4X LDS sample buffer to a final concentration of 1X.

Immunoblotting

Samples from the gel-based orthogonal assay were separated on 4–12% Bis-Tris gels using 1× NuPAGE MES-SDS running buffer. Proteins were transferred to a PVDF membrane, followed by blocking with 5% nonfat dry milk in 1× TBST overnight at 4°C. The membrane was probed with anti-PAN-ADPr antibody (Millipore, MABE1016) for 1 hour at room temperature, followed by three 5-minute TBST-T washes. A secondary anti-rabbit IgG antibody conjugated with IRDye 800 was then applied for 1 hour at room temperature. Signals were visualized using the LI-COR Odyssey M imaging system and quantified with Image Studio software.

Cellular Thermal Shift Assay (CETSA)

SARS-CoV-2 Mac1 (15) was cloned into the pBiT3.1C vector (Promega) with an N-terminal 3×FLAG tag and a C-terminal HiBiT tag. The construct was reverse transfected into U2OS cells using Lipofectamine 3000 (Thermo Fisher). After 48 hours, cells were harvested by trypsinization and resuspended in 1× CETSA buffer containing 1× DPBS, 1 g/L glucose, and 1× protease inhibitor at a density of 10^6 cells/mL. Cells were treated with varying concentrations of GS-441524 or DMSO (final 0.5%) and incubated at 37°C for 1 hour. Samples (40 μL) were aliquoted into PCR strips and heat-stressed at

View Article Online
DOI: 10.1039/D6CB00139D

temperatures ranging from 37°C to 62°C for 3.5 minutes using a preheated thermal cycler, followed by equilibration at room temperature for 10 minutes. For luminescence measurement, 30 µL of the samples was transferred to a 96-well plate and mixed with 30 µL of HiBiT lytic reagent containing LgBiT (Promega). The mixture was incubated for 10 minutes at room temperature, and luminescence was subsequently measured according to the manufacturer's instructions. Luminescence values were normalized to the 37°C DMSO control, and T_{agg} values were determined by fitting the data to a four-parameter sigmoidal equation using non-linear regression in GraphPad Prism. ΔT_{agg} values were calculated as $T_{agg(drug)}$-$T_{agg(DMSO)}$.

To assess protein solubility after heat stress using western blot, cells were lysed using repeated freeze-thaw cycles (four cycles of freezing in a dry ice–ethanol bath for 3 minutes followed by thawing at 37°C for 3 minutes). Lysates were centrifuged at 15,200 × g for 20 minutes at 4°C to separate the soluble and insoluble fractions. The soluble fraction was collected and analyzed by immunoblotting as described above using anti-HiBiT antibody (Promega, 1:1000) for 1 hour at room temperature.

Alphascreen

The AlphaScreen reactions were carried out in 384-well plates (Alphaplate, PerkinElmer, Waltham, MA) in a total volume of 40 µL in buffer containing 25 mM HEPES (pH 7.4), 100 mM NaCl, 0.5 mM TCEP, 0.1% BSA, and 0.05% CHAPS. All reagents were prepared as 4X stocks, and 10 µL volume of each reagent was added to a final volume of 40 µL. All compounds were transferred acoustically using ECHO 555 (Beckman Inc) and preincubated after mixing with purified His-tagged macrodomain protein (250 nM) for 30 min at RT, followed by addition of a 10 amino acid biotinylated and ADP-ribosylated peptide [ARTK(Bio)QTARK(Aoa-RADP)S] (Cambridge peptides) (625 nM). After 1h incubation at RT, streptavidin-coated donor beads (7.5 µg/mL) and nickel chelate acceptor beads (7.5 µg/mL); (PerkinElmer AlphaScreen Histidine Detection Kit) were added under low light conditions, and plates were shaken at 400 rpm for 60 min at RT protected from light. Plates were kept covered and protected from light at all steps and read on BioTek plate reader using an AlphaScreen 680 excitation/570 emission filter set. For counter screening of the compounds, 25 nM biotinylated and hexahistidine-tagged linker peptide (Bn-His_6) (PerkinElmer) was added to the compounds, followed by the addition of beads as described above. For data analysis, the percent inhibition was normalized to positive (DMSO + labeled peptide) and negative (DMSO + macrodomain + peptide, no ADPr) controls. The IC_{50} values were calculated via four-parametric non-linear regression analysis constraining bottom (=0), top (=100), & Hillslope (=1) for all curves.

DSF

View Article Online
DOI: 10.1039/D6CB00139D

Thermal shift assay with DSF involved the use of LightCycler® 480 Instrument (Roche Diagnostics). In total, a 15 µL mixture containing 8X SYPRO Orange (Invitrogen), and 10 µM macrodomain protein in buffer containing 20 mM HEPES-NaOH, pH 7.5, and various concentrations of ADP-ribose or hit compounds was mixed on ice in 384-well PCR plate (Roche). Fluorescent signals were measured from 25 to 95 °C in 0.2 °C/min steps (excitation, 470-505 nm; detection, 540-700 nm). The main measurements were carried out in triplicate. Data evaluation and T_m determination involved use of the Roche LightCycler® 480 Protein Melting Analysis software, and data fitting calculations involved the use of single site binding curve analysis on GraphPad Prism. The thermal shift (ΔT_m) was calculated by subtracting the T_m values of the DMSO from the T_m values of compounds.

Docking of ligands and visualization

The SARS-CoV-2 macrodomain was prepared for ligand docking using make_recepter from the OEDocking 4.3.4 (OEDOCKING 4.3.4.3. OpenEye, Cadence Molecular Sciences, Inc., Santa Fe, NM. http://www.eyesopen.com.) software package, selecting the APR binding site with a cushion of 8 Å around it. The ligands were passed through Omega2 version 6.1.1 (33) for an exhaustive conformer generation. The receptor and conformers were then docked using FRED and a high-resolution grid (1Å translational and rotational stepwise) using the MMFF94 forcefield (34,35).

Additionally, we employed de novo structure and ligand prediction using Boltz2 (36) with the sequence of SARS-CoV-2 Macrodomain. The docked and predicted poses were almost identical with minor shifts <0.2 Å R.M.S.D. The docked poses and crystal structure were visualized using Vida 5.0.7 (OpenEye, Cadence Molecular Sciences, Santa Fe, NM).

Figure legends:

Figure 1: *GS-441524 selectively inhibits the SARS-CoV-2 Mac1 and engages with Mac1 in cells.* A) Schematic representation of the ADPr-Glo assay. B) ADPr-Glo assay dose response of GS-441524 with 4 viral (CHIKV, SARS-CoV, SARS-CoV-2, and MERS-CoV) and 1 human macrodomain (MacroD2). The plotted values are mean ± SD

View Article Online
DOI: 10.1039/D6CB00139D

(n=8). C) Schematic of CETSA. D) Thermal profiles of the SARS-CoV-2 Mac1 and MERS-CoV Mac1 treated with either DMSO or 100 μM GS-441524 or 250 μM GS-441524, indicating an increase in solubility in the presence of GS-441524 for SARS-CoV-2 Mac1, but not for MERS-CoV Mac1. Each point of the plot represents the mean±SD (SARS-CoV-2 n=4; MERS-CoV, n=3). Data were fitted with a sigmoidal dose-response equation using non-linear regression, and the ΔT_{agg} values represent $T_{agg(drug)}$-$T_{agg(DMSO)}$. E) Western blot showing a dose-dependent stabilization of SARS-CoV-2 Mac1 but not MERS-CoV Mac1 at different temperatures using anti-HiBiT antibody. The lower panel presents quantification of the western blot data for SARS-CoV-2 Mac1 (n = 3) and MERS-CoV Mac1 (n = 2) at the corresponding temperature points shown in the blot.

Figure 2: *GS-441524-DP is a more potent inhibitor than its parent component for the SARS-CoV-2 Mac1.* A) Chemical structure of GS-441524 and its phosphorylated derivatives. B) Alphascreen assay showing percent inhibition of alphacounts as a result of binding of GS-441524 and its phosphorylated derivative to SARS-CoV-2 Mac1. Data were fitted using a three-parameter non-linear regression (sigmoidal curve). Data points represent mean ± SD (n=3). C) Thermal stabilization (ΔT□) of Mac1 in the presence of GS-441524 or its phosphorylated derivatives, measured by differential scanning fluorimetry. Bars represent mean ± SD (n = 3). **** P value <0.0001 and ** P value <0.01, using 2-way Anova multiple comparison (GraphPad). D) Western blot showing inhibition of Mac1, indicated by increased ADP-ribosylated substrate signal upon treatment with GS-441524 or its phosphorylated derivatives compared with DMSO control. A representative blot is shown from 3 independent experiments. E) Quantification of ADPr-Substrate signal from (E), normalized to the “no Mac1” control. Bars represent mean ± SD (n=3). **** P value <0.0001 and * P value <0.05, using One-way Anova multiple comparison (GraphPad).

Figure 3: *Docking poses of GS-4415424 and GS-441524-DP compared with ADP-ribose-bound SARS-CoV-2 Mac1*. A) Surface representation of SARS-CoV-2 Mac1 highlighting the adenosine subsite (blue), phosphate tunnel (yellow), distal ribose site (pink), and oxyanion subsite (red). B) Predicted binding pose of GS-4414254 shown in sticks with the ligand meshed contour in orange. C) Predicted binding pose of GS-4414254-DP shown in sticks with the ligand meshed contour in blue. Residues contacting each ligand are shown in green sticks. D) Crystal structure of ADP-ribose-bound SARS-CoV-2 Mac1 (PDB ID:7CZ4) with the ligand contour in black. E) Overlay of the docked ligands (GS-441524, orange; GS-441524-DP, blue) with the ADPr-bound structure (black), showing the relative orientation of each ligand within the active site. F) Root mean square deviation (R.M.S.D.) of C_α atoms in Mac1 docked with GS-441524

View Article Online
DOI: 10.1039/D6CB00139D

and GS-441524-DP compared to the ADP-ribose bound Mac1 structure (PDB: 7CZ4).

Author Contribution

Banhi Biswas: Conceptualization; Resources; Formal analysis; Supervision; Validation; Investigation; Visualization; Writing—original draft; Writing—review and editing. **Junlin Zhuo:** Conceptualization; Formal analysis; Validation; Investigation; Visualization; Writing—review and editing. **Jürgen Bosch:** Formal analysis; Validation; Investigation; Visualization; Writing—review and editing. **Hien Vu:** Formal analysis; Validation; Investigation; Writing—review and editing. **Lorencia Pak:** Formal analysis; Investigation. **Rameez Raja:** Formal analysis; Investigation. **Anuradha Roy:** Formal analysis; Validation; Investigation; Visualization; Writing—review and editing. **Alessandro Panattoni:** Formal analysis; Validation; Investigation; Visualization; Writing—review and editing. **Michal Maryska:** Formal analysis; Validation; Investigation; Visualization; Writing—review and editing. **Petr Slavik:** Formal analysis; Validation; Investigation; Visualization; Supervision; Writing—review and editing. **Kryštof Šigut:** Supervision; Writing—review and editing. **Anthony R. Fehr:** Supervision; Funding acquisition; Writing—review and editing. **Rachy Abraham:** Formal analysis; Writing—review and editing. **Barbara S. Slusher:** Supervision; Writing—review and editing. **Takashi Tsukamoto:** Supervision; Writing—review and editing. **Anthony K.L. Leung:** Conceptualization; Supervision; Funding acquisition; Visualization; Writing—original draft; Project administration; Writing—review and editing.

Conflicts of interest

SigutLabs is a chemical CRO providing various nucleotides (including Remdesivir monophosphate, Remdesivir diphosphate, Remdesivir triphosphate).

Data availability

The data supporting this article have been included as part of the Supplementary Information.

Acknowledgement

This work is supported by Novo Nordisk Foundation NNF24SA0091940 (A.K.L.L.) and NIH P20GM113117 (A.F).

References

1. Rack JGM, Perina D, Ahel I. Macrodomains: structure, function, evolution, and catalytic activities. Annu Rev Biochem. 2016;85(1):431–54.

View Article Online
DOI: 10.1039/D6CB00139D

2. Leung AKL, Griffin DE, Bosch J, Fehr AR. The conserved macrodomain is a potential therapeutic target for coronaviruses and alphaviruses. Pathogens. 2022;11(1):94.

3. Fehr AR, Jankevicius G, Ahel I, Perlman S. Viral macrodomains: unique mediators of viral replication and pathogenesis. Trends Microbiol. 2018;26(7):598–610.

4. Leung AKL, McPherson RL, Griffin DE. Macrodomain ADP-ribosylhydrolase and the pathogenesis of infectious diseases. PLoS Pathog. 2018;14(3):e1006864.

5. Hoch NC. Host ADP-ribosylation and the SARS-CoV-2 macrodomain. Biochem Soc Trans. 2021;49(4):1711–21.

6. Daugherty MD, Young JM, Kerns JA, Malik HS. Rapid evolution of PARP genes suggests a broad role for ADP-ribosylation in host-virus conflicts. PLoS Genet. 2014;10(5):e1004403.

7. McPherson RL, Abraham R, Sreekumar E, Ong SE, Cheng SJ, Baxter VK, et al. ADP-ribosylhydrolase activity of Chikungunya virus macrodomain is critical for virus replication and virulence. Proceedings of the National Academy of Sciences. 2017;114(7):1666–71.

8. Fehr AR, Channappanavar R, Jankevicius G, Fett C, Zhao J, Athmer J, et al. The conserved coronavirus macrodomain promotes virulence and suppresses the innate immune response during severe acute respiratory syndrome coronavirus infection. mBio. 2016;7(6):10–1128.

9. Alhammad YM, Parthasarathy S, Ghimire R, Kerr CM, O'Connor JJ, Pfannenstiel JJ, et al. SARS-CoV-2 Mac1 is required for IFN antagonism and efficient virus replication in cell culture and in mice. Proceedings of the National Academy of Sciences. 2023;120(35):e2302083120.

10. Taha TY, Suryawanshi RK, Chen IP, Correy GJ, McCavitt-Malvido M, O'Leary PC, et al. A single inactivating amino acid change in the SARS-CoV-2 NSP3 Mac1 domain attenuates viral replication in vivo. PLoS Pathog. 2023;19(8):e1011614.

11. Kerr CM, Pfannenstiel JJ, Alhammad YM, O'Connor JJ, Ghimire R, Shrestha R, et al. Mutation of a highly conserved isoleucine residue in loop 2 of several β-coronavirus macrodomains indicates that

View Article Online
DOI: 10.1039/D6CB00139D

enhanced ADP-ribose binding is detrimental for replication. J Virol. 2024;98(11):e01313-24.

12. O'Connor JJ, Ferraris D, Fehr AR. An update on the current state of SARS-CoV-2 Mac1 inhibitors. Pathogens. 2023;12(10):1221.

13. Schuller M, Correy GJ, Gahbauer S, Fearon D, Wu T, Díaz RE, et al. Fragment binding to the Nsp3 macrodomain of SARS-CoV-2 identified through crystallographic screening and computational docking. Sci Adv. 2021;7(16):eabf8711.

14. Gahbauer S, Correy GJ, Schuller M, Ferla MP, Doruk YU, Rachman M, et al. Iterative computational design and crystallographic screening identifies potent inhibitors targeting the Nsp3 macrodomain of SARS-CoV-2. Proceedings of the National Academy of Sciences. 2023;120(2):e2212931120.

15. Suryawanshi RK, Jaishankar P, Correy GJ, Rachman MM, O'Leary PC, Taha TY, et al. The Mac1 ADP-ribosylhydrolase is a therapeutic target for SARS-CoV-2. bioRxiv. 2024.

16. Wazir S, Parviainen TAO, Pfannenstiel JJ, Duong MTH, Cluff D, Sowa ST, et al. Discovery of 2-amide-3-methylester thiophenes that target SARS-CoV-2 Mac1 and repress coronavirus replication, validating Mac1 as an antiviral target. J Med Chem. 2024;67(8):6519–36.

17. Sherrill LM, Joya EE, Walker A, Roy A, Alhammad YM, Atobatele M, et al. Design, synthesis and evaluation of inhibitors of the SARS-CoV-2 nsp3 macrodomain. Bioorg Med Chem. 2022;67:116788.

18. Ni X, Schröder M, Olieric V, Sharpe ME, Hernandez-Olmos V, Proschak E, et al. Structural insights into plasticity and discovery of remdesivir metabolite GS-441524 binding in SARS-CoV-2 macrodomain. ACS Med Chem Lett. 2021;12(4):603–9.

19. Tsika AC, Gallo A, Fourkiotis NK, Argyriou AI, Sreeramulu S, Loehr F, et al. Binding adaptation of GS-441524 diversifies Macro domains and downregulates SARS-CoV-2 de-MARylation capacity. J Mol Biol. 2022;434(16):167720.

20. Peng K, Wallace SD, Bagde SR, Shang J, Anmangandla A, Jana S, et al. GS-441524-Diphosphate-Ribose Derivatives as Nanomolar Binders and Fluorescence Polarization Tracers for SARS-CoV-2 and Other Viral Macrodomains. ACS Chem Biol. 2024;19(5):1093–105.

View Article Online
DOI: 10.1039/D6CB00139D

21. Dasovich M, Zhuo J, Goodman JA, Thomas A, McPherson RL, Jayabalan AK, et al. High-throughput activity assay for screening inhibitors of the SARS-CoV-2 Mac1 macrodomain. ACS Chem Biol. 2021;17(1):17–23.

22. Tao S, Zandi K, Bassit L, Ong YT, Verma K, Liu P, et al. Comparison of anti-SARS-CoV-2 activity and intracellular metabolism of remdesivir and its parent nucleoside. Current research in pharmacology and drug discovery. 2021;2:100045.

23. Xie X, Muruato AE, Zhang X, Lokugamage KG, Fontes-Garfias CR, Zou J, et al. A nanoluciferase SARS-CoV-2 for rapid neutralization testing and screening of anti-infective drugs for COVID-19. Nat Commun. 2020;11(1):5214.

24. Li Y, Cao L, Li G, Cong F, Li Y, Sun J, et al. Remdesivir metabolite GS-441524 effectively inhibits SARS-CoV-2 infection in mouse models. J Med Chem. 2021;65(4):2785–93.

25. Stevens LJ, Pruijssers AJ, Lee HW, Gordon CJ, Tchesnokov EP, Gribble J, et al. Mutations in the SARS-CoV-2 RNA-dependent RNA polymerase confer resistance to remdesivir by distinct mechanisms. Sci Transl Med. 2022;14(656):eabo0718.

26. Chen Z, Boon SS, Wang MH, Chan RWY, Chan PKS. Genomic and evolutionary comparison between SARS-CoV-2 and other human coronaviruses. J Virol Methods. 2021;289:114032.

27. Martinez NJ, Asawa RR, Cyr MG, Zakharov A, Urban DJ, Roth JS, et al. A widely-applicable high-throughput cellular thermal shift assay (CETSA) using split Nano Luciferase. Sci Rep. 2018;8(1):9472.

28. Roy A, Alhammad YM, McDonald P, Johnson DK, Zhuo J, Wazir S, et al. Discovery of compounds that inhibit SARS-CoV-2 Mac1-ADP-ribose binding by high-throughput screening. Antiviral Res. 2022;203:105344.

29. Alhammad YMO, Kashipathy MM, Roy A, Gagné JP, McDonald P, Gao P, et al. The SARS-CoV-2 conserved macrodomain is a mono-ADP-ribosylhydrolase. J Virol. 2021;95(3):10–1128.

30. DeLano WL. Pymol: An open-source molecular graphics tool. CCP4 Newsl protein crystallogr. 2002;40(1):82–92.

View Article Online
DOI: 10.1039/D6CB00139D

31. Krishnathas R, Mineev KS, Fourkiotis NK, Touret F, Sideras-Bisdekis C, Tsika AC, et al. Structure-Based Rational Design of a Selective Hydrolase Inhibitor of the Severe Acute Respiratory Syndrome Coronavirus-2 Nsp3 Macrodomain. ChemBioChem. 2025;26(23):e202500593.

32. Rijpkema KJ, Schuller M, van der Veer MS, Rieken S, Chang DLR, Balić P, et al. Synthesis of Structural ADP-Ribose Analogues as Inhibitors for SARS-CoV-2 Macrodomain 1. Org Lett. 2024;26(27):5700–4.

33. Hawkins PCD, Skillman AG, Warren GL, Ellingson BA, Stahl MT. Conformer generation with OMEGA: algorithm and validation using high quality structures from the Protein Databank and Cambridge Structural Database. J Chem Inf Model. 2010;50(4):572–84.

34. McGann M. FRED pose prediction and virtual screening accuracy. J Chem Inf Model. 2011;51(3):578–96.

35. McGann M. FRED and HYBRID docking performance on standardized datasets. J Comput Aided Mol Des. 2012;26(8):897–906.

36. Passaro S, Corso G, Wohlwend J, Reveiz M, Thaler S, Somnath VR, et al. Boltz-2: Towards accurate and efficient binding affinity prediction. BioRxiv. 2025.

View Article Online
DOI: 10.1039/D6CB00139D

Figure 1

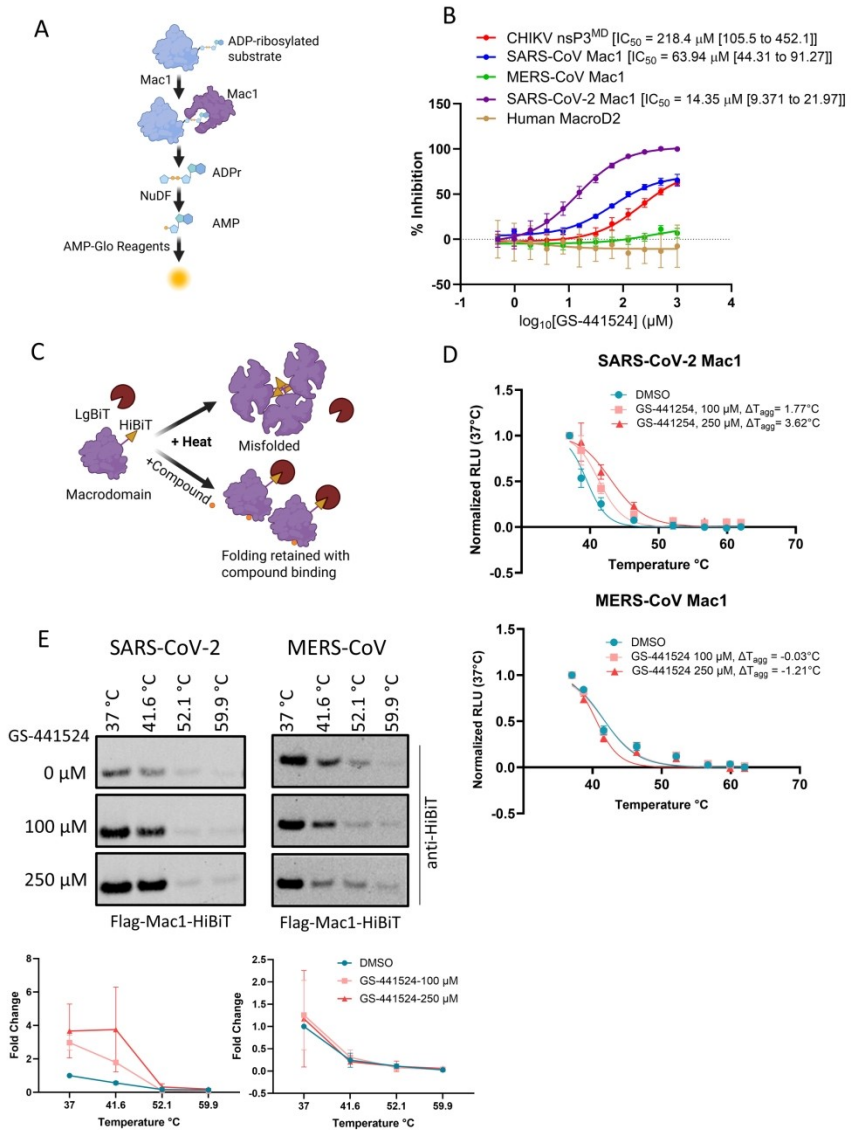

190x254mm (300 x 300 DPI)

View Article Online
DOI: 10.1039/D6CB00139D

Figure 2

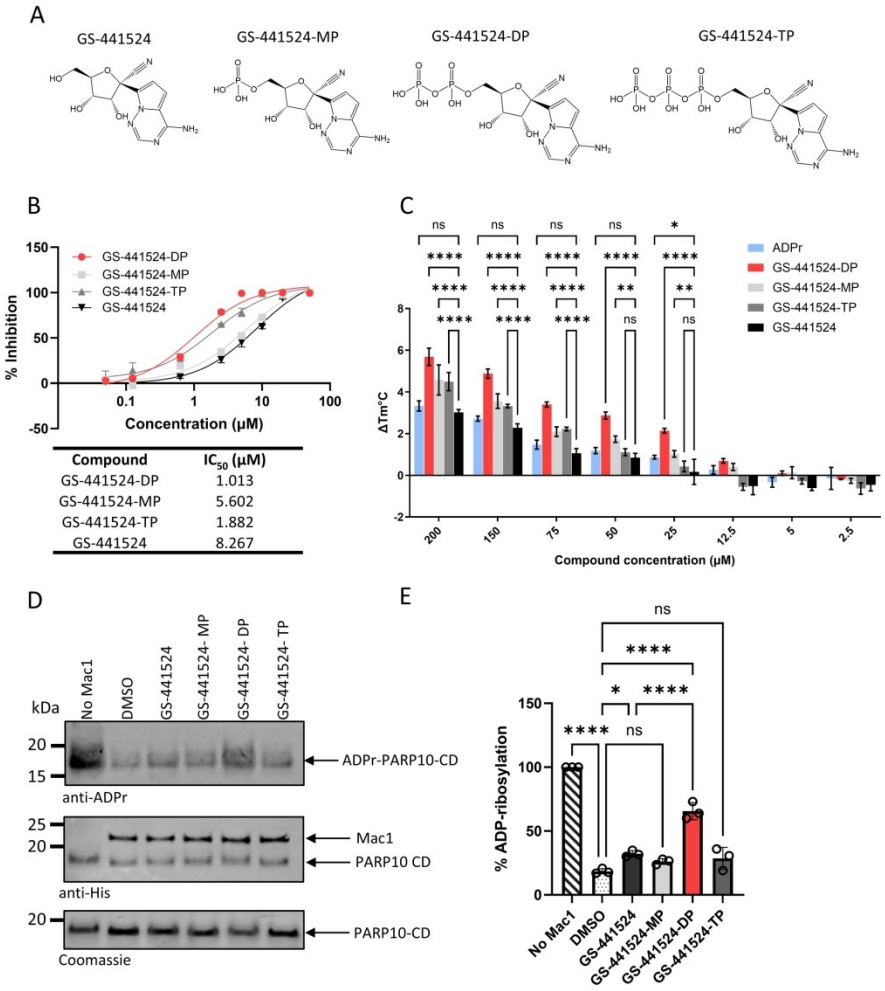

190x254mm (300 x 300 DPI)

View Article Online
DOI: 10.1039/D6CB00139D

Figure 3

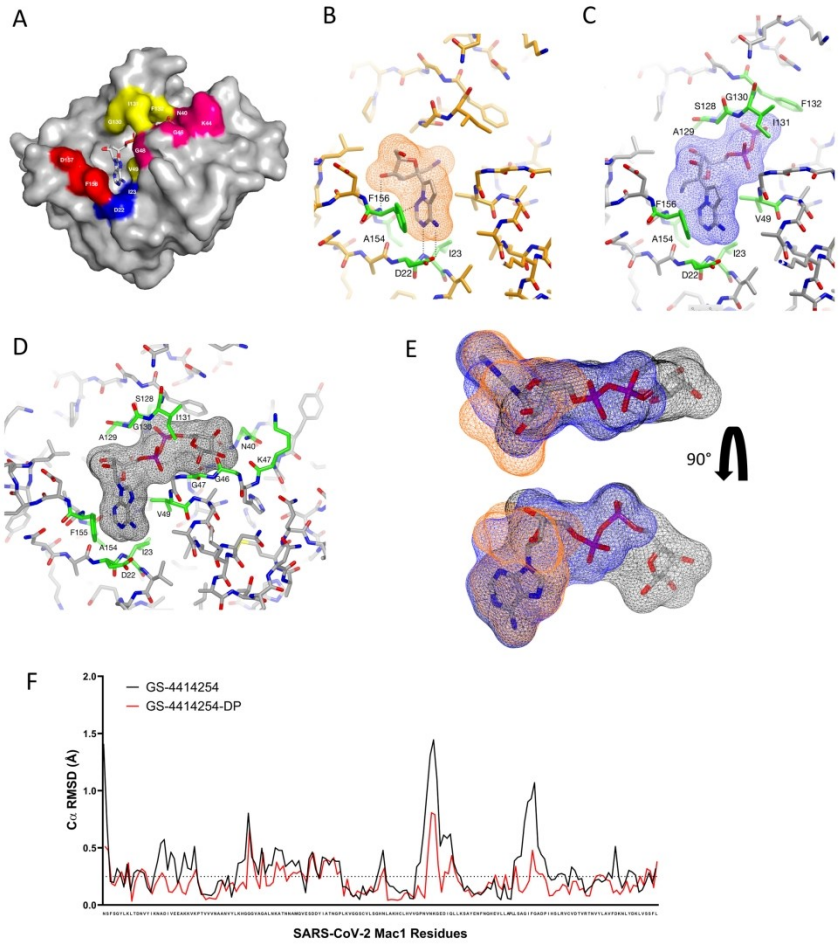

190x254mm (300 x 300 DPI)

View Article Online
DOI: 10.1039/D6CB00139D

Data availability

The data supporting this article have been included as part of the Supplementary Information.